Title

Degradation Mechanism of Phosphate-Based Li-NASICON Conductors in Alkaline Environment

Authors

Lam, Benjamin X
Li, Zhuohan
Mishra, Tara P
et al.

Publication Date

2024

DOI

10.1002/aenm.202403596

ADVANCED ENERGY MATERIALS
www.advenergymat.de

Degradation Mechanism of Phosphate-Based Li-NASICON Conductors in Alkaline Environment

*Benjamin X. Lam, Zhuohan Li, Tara P. Mishra, and Gerbrand Ceder**

NASICON-type Li conductors (Li-NASICON) have traditionally been regarded as promising candidates for solid-state Li-air battery applications because of their stability in water and ambient air. However, the presence of water in the cathode of a Li-air battery can induce a highly alkaline environment by modifying the discharge product from Li_2O_2 to LiOH which can potentially degrade cathode and separator materials. This study investigates the alkaline stability of common Li-NASICON chemistries through a systematic experimental study of $LiTi_xGe_{2-x}(PO_4)_3$ (LTGP) with varying x = 0–2.0. Density functional theory calculations are combined to gain a mechanistic understanding of the alkaline instability. It is demonstrated that the instability of LTGP in an alkaline environment is mainly driven by the dissolution of PO_4^{3-} groups, which subsequently precipitate as Li_3PO_4. The introduction of Ti facilitates the formation of a Ti-rich compound on the surface that eventually passivates the material, but only after significant bulk degradation. Consequently, phosphate-based Li-NASICON materials exhibit limited alkaline stability, raising concerns about their viability in humid Li-air batteries.

1. Introduction

Li-air batteries have the highest specific energy among all "beyond Li-ion" battery systems[1] with a theoretical specific energy of >3000 and >2000 Wh kg^{-1} for Li_2O_2 and $LiOH{\cdot}H_2O$ as the discharge product, respectively.[2] These batteries operate by oxidizing Li at the anode and reducing oxygen gas at the cathode to grow lithium-oxygen discharge products within a porous cathode structure.[3] Ideally, ambient air would be used as the oxygen source. However, Li-air battery research currently operates in ideal conditions, commonly only using O_2 gas in the cathode to prevent parasitic reactions with CO_2 and H_2O in the air.[4] In order to create a true "Li-air" battery, resilience to reactions generated by both CO_2 and H_2O must be considered. CO_2 is considered a contaminant because the Li_2O_2 discharge product reacts to form Li_2CO_3 which is very stable and leads to a high oxidation potential on charge.[4,5] Some researchers have elected to use water as a beneficial additive because the introduction of water into the cathode alters the morphology and phase of discharge products by encouraging the growth of larger Li_2O_2 crystals, thereby increasing the discharge capacity.[6–11] These crystals are then chemically converted to LiOH in the presence of water and can aid in reducing the charge overpotential since LiOH has higher ionic and electronic conductivity than Li_2O_2.[7,12–15] In the extreme case, the cathode gas can be at saturated humidity and LiOH may be produced directly from a 4-electron process, leading to a higher discharge potential of 3.4V.[16]

A challenge for the operation in humidity is that LiOH quickly absorbs water when the relative humidity is above 20%.[17,18] In such environments, LiOH can partially dissolve and expose the surrounding material to a highly alkaline environment. In-situ optical microscopy investigations into the discharge mechanism of humidified Li-O_2 batteries have shown that large droplets of hydrated LiOH grow as the battery is discharged.[19] The hydration level was estimated to exceed $LiOH{\cdot}9.5H_2O$, which is near the solubility limit of LiOH in water,[20] confirming that a highly alkaline environment is generated. Therefore, both separator and cathode materials must be resistant to alkaline solutions when water is present.

Among the many types of superionic conductors, NASICON-type Li conductors (Li-NASICON) stand out as one class of materials that may function as an appropriate separator or catholyte because of their stability in water and ambient air.[21–24] In comparison to polymer, garnet, perovskite, and sulfide solid-state electrolytes, NASICONs have the best chemical stability in ambient air.[25] Previous studies on $Li_{1.3}Al_{0.3}Ti_{1.7}(PO_4)_3$ (LATP) stability in alkaline environment have reported small amounts of Li_3PO_4 or $AlPO_4$ impurities presumably forming at grain boundaries, leading to a decrease in ionic conductivity.[22,26] $Li_{1.3}Al_{0.3}Ge_{1.7}(PO_4)_3$ (LAGP) also experiences a decrease in total conductivity when exposed to an alkaline environment.[27,28]

B. X. Lam, G. Ceder
Department of Materials Science and Engineering
University of California
210 Hearst Memorial Mining Building, Berkeley, CA 94720, USA
E-mail: gceder@berkeley.edu
Z. Li, T. P. Mishra, G. Ceder
Materials Science Division
Lawrence Berkeley National Laboratory
1 Cyclotron Road, Berkeley, CA 94720, USA

The ORCID identification number(s) for the author(s) of this article can be found under https://doi.org/10.1002/aenm.202403596

DOI: 10.1002/aenm.202403596

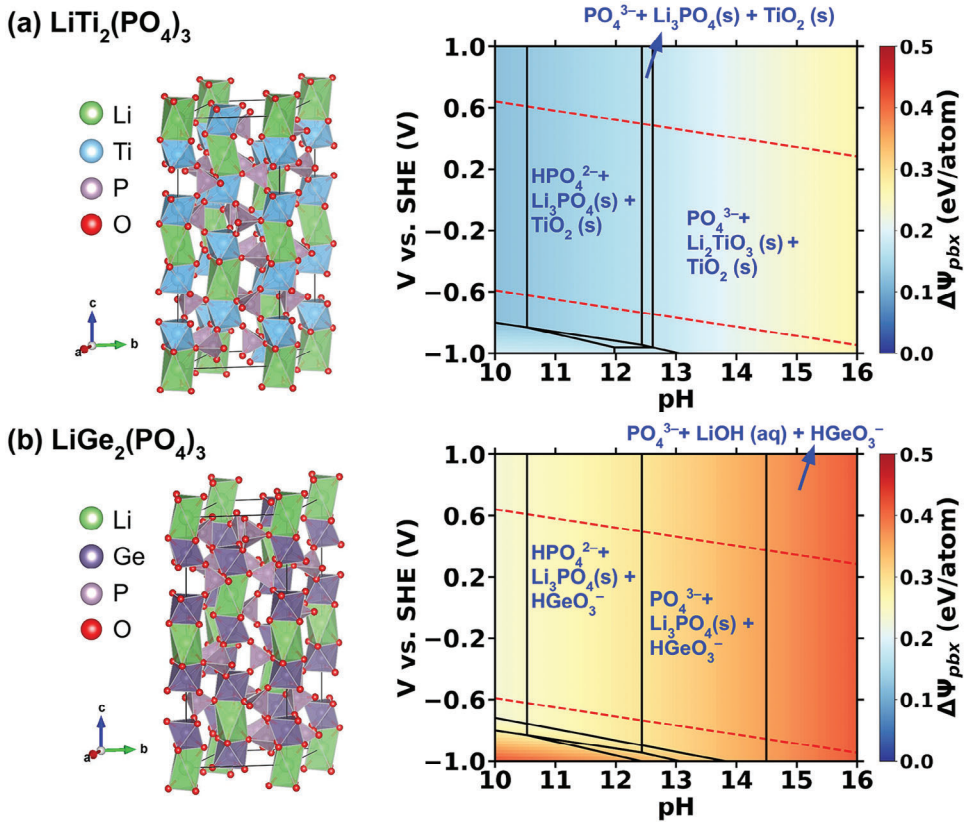

Figure 1. Ab-initio calculated Pourbaix diagrams for a) $LiTi_2(PO_4)_3$ (LTP), b) $LiGe_2(PO_4)_3$ (LGP). The crystal structures are shown on the left. The color scheme in the computed Pourbaix diagrams (on the right) represents the Pourbaix decomposition energy $\Delta\Psi_{pbx}$ with respect to the convex hull of Pourbaix potential. The concentration of Li^+ ions is set to 0.5 mol L^{-1}, while the concentrations of all other ionic species are set to 10^{-6} mol L^{-1}, in order to imitate the initial condition of the experiments. In each domain, the most stable phases of the system are shown, including both solid phases and dissolved species. Red dashed lines are the water stability limits.

In order to design new materials for this harsh environment, a mechanistic understanding of the alkaline stability of Li-NASICON materials is needed. In this study, we use $LiTi_xGe_{2-x}(PO_4)_3$ (LTGP) as a model material to yield insight into the alkaline stability of similar Li-NASICONs. Degradation products were identified by combining diffraction and spectroscopic techniques while density functional theory (DFT) calculations were used to determine the thermodynamic driving force for the decomposition of Li-NASICON in high pH solutions. We find that for the compositions tested, the dissolution of PO_4^{3-} groups dominates the driving force for decomposition. Further, we find that substituting Ge with Ti can mitigate dissolution by forming a Ti-rich oxide as a surface passivation layer. This study systematically investigates the degradation mechanism and behavior of LTGP, revealing the fundamental challenges of using phosphate-based Li-NASICONs in highly alkaline environments commonly encountered in Li-air batteries with water exposure.

2. Results

2.1. Ab-Initio Pourbaix Diagram: Thermodynamic Stability of $LiTi_2(PO_4)_3$ and $LiGe_2(PO_4)_3$

We aim to investigate how the chemistry on the octahedral M sites in a NASICON-type structure ($LiM_2(PO_4)_3$) affects the stability in an alkaline environment. Ti and Ge are chosen as representative metals because of their relevance as common elements in Li-NASICON solid electrolytes, i.e., LATP and LAGP, where Al is used to increase the Li-concentration so that a higher Li conductivity can be achieved.[29] A previous study indicated that Ti and Ge can form a solid solution in the Li-NASICON framework spanning the entire composition range of LTGP ($LiTi_xGe_{2-x}(PO_4)_3$, $0 \leq \times \leq 2$).[30] In this study, we will systematically examine the alkaline stability of LTGP with varying Ti/Ge composition.

We computationally evaluate the alkaline stability of LTP and LGP by constructing Pourbaix diagrams using density functional theory (DFT) following the formalism of Persson et al.[31] A Pourbaix diagram reveals whether a target composition is thermodynamically stable at a given pH and voltage, and if not, what solid phases or dissolved species it may decompose into. The voltage is a measure of the energetic cost of electrons and in these diagrams is referenced against the standard hydrogen electrode (SHE). The ab-initio Pourbaix diagrams of LTP and LGP obtained by our calculations are shown in **Figure 1**. Our calculations predict that, at high pH conditions, both LTP and LGP are not thermodynamically stable and will decompose into combinations of solids and dissolved ions.

The decomposition of LGP is predicted to result in the dissolution of P as phosphate ions (PO_4^{3-} or HPO_4^{2-}) and Ge as

$HGeO_3^-$. The only solid phase that appears in the Pourbaix diagram of LGP is Li_3PO_4, whose formation is driven by the high Li concentration (0.5 mol L^{-1}). This Li concentration is significantly higher than the Li concentration of a saturated Li_3PO_4 solution (<0.01 mol L^{-1}) in the pH range of 11–13.[32] Such a high Li concentration was set as the initial condition of our experiments, as well as in our ab-initio Pourbaix diagram calculations, in order to mimic the environment of the cathode surface of a humidified Li-air battery cell at the end of discharge. The decomposition of LTP is similarly predicted to result in the dissolution of P as phosphate ions and Li_3PO_4 formation, but LTP is also expected to decompose into additional solid phases TiO_2 or Li_2TiO_3, depending on pH.

The driving force for the decomposition reaction, $\Delta\Psi_{pbx}$, can be estimated by calculating the difference in the Pourbaix potential between the target composition (LTP or LGP) and the decomposition products with the lowest energy at a given pH and voltage.[33,34] $\Delta\Psi_{pbx}$ is represented as a colormap in Figure 1 and clearly shows that LGP has a much larger tendency to decompose (larger $\Delta\Psi_{pbx}$) compared to that of LTP. At our experimental condition of pH = 12 (assuming V = 0 V vs SHE), the Pourbaix decomposition energy for LTP is $\Delta\Psi_{pbx}$ = 0.1565 eV/atom, while $\Delta\Psi_{pbx}$ = 0.2801 eV/atom for LGP — almost twice that of LTP. A previous study showed that a material can be stable in a solution if either 1) the Pourbaix decomposition energy is low, or 2) the material forms a stable solid phase at a given pH and voltage condition to passivate the surface.[33] While both LTP and LGP are predicted to decompose into solid Li_3PO_4, we hypothesize that the appearance of additional solid phases in LTP decomposition (TiO_2 or Li_2TiO_3) may enhance the material's protection against continuous dissolution. Additionally, the lower decomposition energy of LTP may indicate that LTP can dissolve at a lower rate than LGP, rendering LTP more stable than LGP in alkaline environments.

2.2. Phase Identification of Alkaline Decomposition Products in $LiTi_xGe_{2-x}(PO_4)_3$

To test our hypothesis, we synthesized a series of LTGP samples with varying Ti fractions, including 0% (LGP), 25% ($LiTi_{0.5}Ge_{1.5}(PO_4)_3$, LTGP25), 50% ($LiTiGe(PO_4)_3$, LTGP50), 75% ($LiTi_{1.5}Ge_{0.5}(PO_4)_3$, LTGP75), and 100% (LTP). These samples were immersed in an alkaline 0.5 mol L^{-1} LiOH solution buffered with 0.25 mol L^{-1} H_3BO_3 with pH 12.3 to examine their alkaline stability. Pristine samples were characterized with XRD and all samples matched the expected Li-NASICON structure with space group R-3c. The lattice constant was found to linearly increase with increasing Ti-content, implying that the Ti is successfully incorporated into the structure (Figure S1, Supporting Information).[30] Additionally, we found a homogenous elemental distribution of Ti and Ge when examined by EDS, confirming that the material is single-phase (Figure S2, Supporting Information).

After 48 h of immersion, the pellet samples were extracted and prepared for powder XRD analysis. Stark macroscopic differences between the pellets could be visually observed. The LGP pellet easily crumbled and the sample lost significant structure after 48 h in solution, with large portions of the pellet dissolving. In contrast, the pellet samples containing Ti (LTGP25, LTGP50, LTGP75, LTP) all remained intact throughout the experiment with no visible changes to them. The XRD spectra of pellet samples after 48 h in solution are shown in **Figure 2a**. The XRD signature of LGP almost completely disappears after the 48 h immersion and is replaced by GeO_2. In LTGP/LTP the XRD peaks for the NASICON phase are maintained and very small peaks belonging to Li_3PO_4 are seen in LTGP25 and LTGP50. We hypothesize that the degradation is localized to the surface of the pellet, so the weak Li_3PO_4 signal is a result of a relatively larger phase fraction of the unreacted bulk material.

Powders have a larger surface-to-volume ratio compared to a pellet, so we expect that the phase fraction of the degraded solid material will become larger and allow easier identification of the degradation products. Figure 2b shows the XRD spectra of LTGP25 powders that have spent various times immersed in solution. As the immersion time increases, the NASICON phase is maintained but an increasing amount of Li_3PO_4 is clearly seen. All compositions tested showed a similar behavior. The growth of the Li_3PO_4 phase over time was quantified with Rietveld refinement with the results shown in Figure 2c. Across all refined powder spectra, the median R_{wp} was 4.60%, indicating a good agreement between the refinement model and experimental data (Figure S3 and Table S1, Supporting Information). The amount of Li_3PO_4 is the highest in LGP, consistent with its predicted poor stability. As Ti is substituted into the NASICON framework, the Li_3PO_4 content is significantly reduced. Surprisingly, LTGP75 shows slightly less Li_3PO_4 formation than LTP. This is likely because the particle size of LTGP75 powders is ≈50% larger in diameter than the other powders, resulting in less reaction in the solution (Figures S2 and S7, Supporting Information). After ≈50 h, the amount of Li_3PO_4 forming appears to taper off, implying a significant slowdown or termination of the reaction.

The XRD patterns of Ti-containing samples were fully indexed to either the Li_3PO_4 or Li-NASICON phases, with the only unmatched peak being a small peak at $2\theta = 28.29°$ (Figure S3, Supporting Information). This signal is strongest in LTP and diminishes with the amount of Ti present in the sample (Table S1, Supporting Information). The Pourbaix diagram shows that the most stable Ti-rich solid phase near the experimental pH condition (pH 12.3) is TiO_2 and we found that this peak best matches the main peak of the monoclinic bronze-phase TiO_2 (TiO_2 (B)).[35] The small intensity from the Ti-rich phase may be due to its morphology as a very thin Ti-rich layer or may indicate that some portion of the Ti-compound is amorphous. These Ti-rich compounds most likely act as a passivation layer, which may be why Ti-containing LTGP/LTP shows less significant degradation than LGP.

2.3. Ionic Dissolution of $LiTi_xGe_{2-x}(PO_4)_3$

The concentration of ions dissolved in the solution was measured by ICP-OES. In **Figure 3**, the amount of each dissolved ion is reported as a fraction of the total amount of that ion present in the system, including both solid material and alkaline solution. This allows us to compare the dissolution behavior over different solid sample compositions.

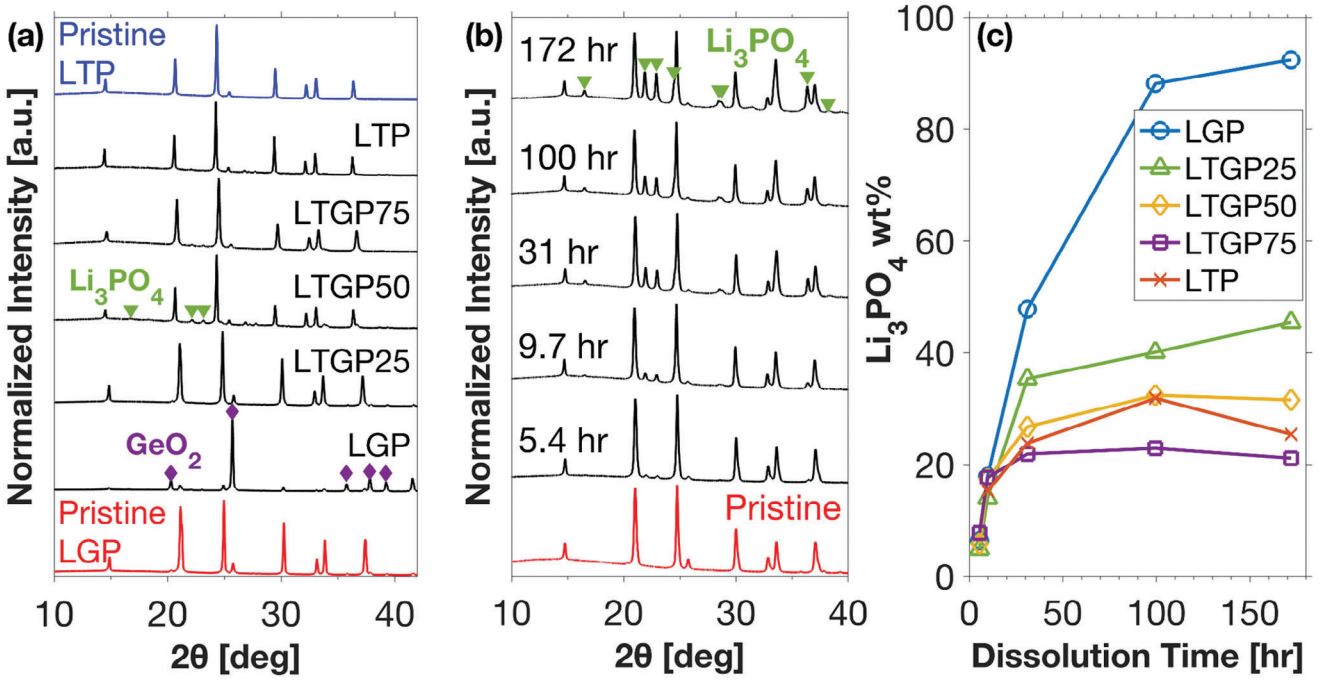

Figure 2. XRD spectra of a) 48-h degraded pellet samples, b) $LiTi_{0.5}Ge_{1.5}(PO_4)_3$ (LTGP25) powder samples as a function of time immersed in solution, and c) refined Li_3PO_4 phase fractions in the powder samples. Spectra shown in (b) were refined to $LiGe_2(PO_4)_3$ (ICSD coll. code 69763) or $LiTi_2(PO_4)_3$ (ICSD coll. code 7930), β-Li_3PO_4 (ICSD coll. code 257439), and TiO_2(B) (ICSD coll. code 41056).

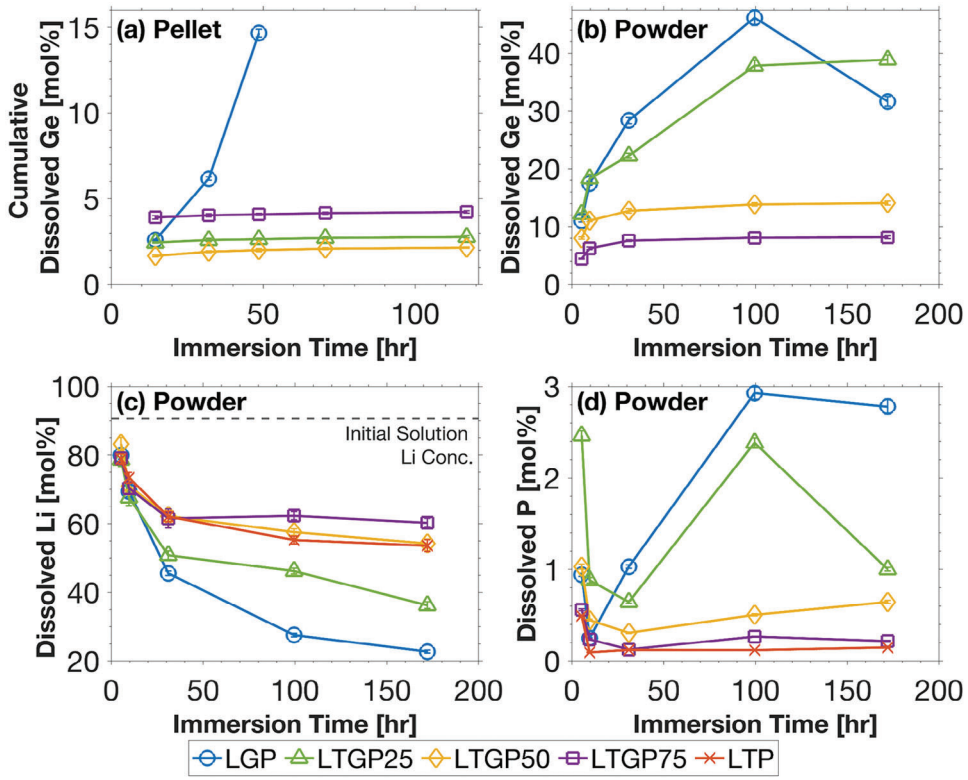

Figure 3. ICP-OES measured ion concentrations in solutions of a) pellet samples and b–d) powder samples normalized to the amount of ion species present in the system. The initial Li concentration in the solution (0.5 mol L^{-1}) is shown by the dashed line in (b). The error bars represent one standard deviation and are smaller than the displayed symbols for most data points.

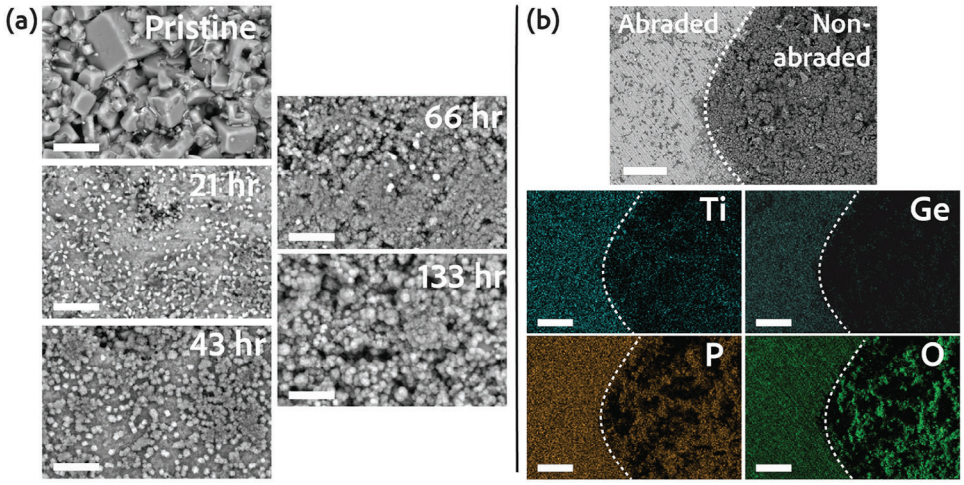

Figure 4. a) SEM images of a LTGP50 pellet after immersion in an alkaline solution at 70 °C at various times. b) SEM/EDS images of a LTGP50 pellet after 116 h of immersion with the surface partially abraded (left side). The abrasion reveals the bulk material underneath the decomposition products allowing comparison between the bulk and decomposition product layer (right side). Scale bars are 10 µm in (a) and 50 µm in (b).

Figure 3a depicts the cumulative mol fraction of Ge dissolved over time for the pellet samples. After 50 h of immersion, 14.6% of the LGP pellet's Ge-ions were dissolved into solution and the dissolution appears unconstrained. The amount of Ge extracted from the LGP pellet is also likely an underestimation since a solid GeO_2 precipitate is observed in XRD, implying that more than 14.6% of Ge-ions in the pellet dissolved, but some reprecipitated as GeO_2. In contrast, the amount of dissolved Ge plateau at values <5 mol% in all samples containing Ti. Nearly no Ti was observed to dissolve into solution (Figure S4, Supporting Information).

Figures 3b–d show the dissolution of ions in powder samples. LGP is again seen to dissolve readily with >40% Ge dissolved after 100 h (Figure 3b). The Ge concentration in the solution of the LGP sample dropped significantly after 100 h, consistent with the precipitation of GeO_2. Again, nearly no Ti dissolved into the solution from the powder samples (Figure S6, Supporting Information). Figure 3c shows the concentration of Li in solution which can be seen to continuously decrease for all powder samples, indicating that Li-ions are removed from the solution due to the precipitation of Li_3PO_4. The shape of the dissolved Li-concentration curve also matches that of the refined XRD phase fractions of Li_3PO_4 shown in Figure 2c, both starting with a high rate of change and leveling out after ≈50 h. In Figure 3d, the P concentration initially increases as some of the LTGP powder is dissolved, then quickly decreases as PO_4^{3-} ions are precipitated as Li_3PO_4. The Li-NASICON phase is the only source of PO_4 in the system, so Li_3PO_4 must be formed by a dissolution-precipitation mechanism.

2.4. Morphology of Decomposition Products

The formation of Li_3PO_4 is further confirmed by the SEM/EDS images of the surface of the LTGP50 pellet that was taken ex-situ after the pellet was immersed in an alkaline solution. **Figure** 4a shows the surface of the LTGP50 pellet at various times. After 21 h, small particles (≈1 µm) form on the surface. By 43 h, the particles have grown in size and eventually cover the entire surface by 66 h.

To enhance the contrast between the top layer of decomposition products and the underlying bulk, a section of the surface of the degraded pellet was abraded with 1200-grit SiC sandpaper to reveal the bulk material (Figure 4b). The abraded section (left side) has a homogeneous distribution of Ti, Ge, P, and O which is indicative of the pristine bulk material and shows that the degradation of the pellet is mainly localized to the surface. The particles that grow to cover the surface are likely Li_3PO_4 because the EDS maps of the nonabraded side (right side) detect P and O, whereas the Ti and Ge intensity appear to be diminished. Further, the continued growth of these particles to a thick layer by 116 h aligns with the growth time scale of the Li_3PO_4 phase observed by XRD (Figure 2).

The diminished intensity of Ti and Ge signals in the decomposition product layer (right side) suggests that there are no Ti or Ge compounds within this product layer. Our ICP-OES experiments showed that while Ge was observed to dissolve into the solution, Ti did not dissolve. Therefore, any solid Ti-compounds that form are most likely present underneath the Li_3PO_4 product layer.

2.5. Computational Simulation of Surface Defect Formation of LTP/LGP

The experimental results show that the alkaline stability of the LTGP series increases as the Ti-content increases, evidenced by the formation of a smaller amount of Li_3PO_4 and less dissolution of Ge into the solution. We conducted DFT calculations on LTP and LGP surfaces to obtain a mechanistic understanding of such improvement in alkaline stability. To gauge the driving force of surface degradation in a high pH solution, we calculated the energy to move ions into the solution and create surface defects. The formation of different types of surface defects, either vacancy or adsorbate, are considered to represent the elemental steps in the early stage of surface degradation.

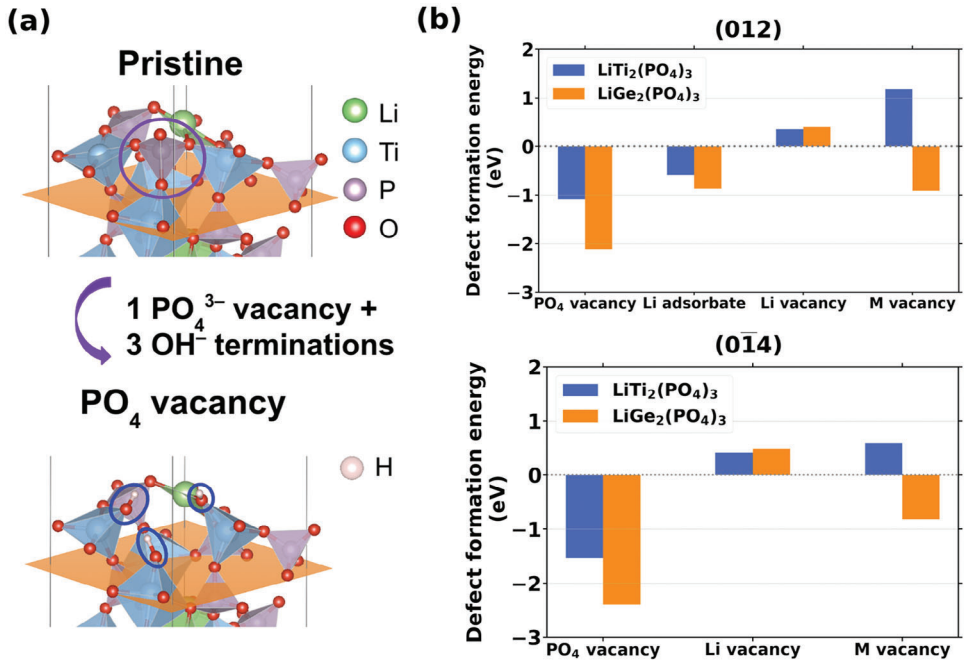

Figure 5. DFT calculation of the thermodynamic driving force for dissolution of ions from the LTP/LGP surfaces. (a) Surface structure of the pristine and the defected LTP (012) surfaces. The PO_4 vacancy is obtained by removing one PO_4^{3-} group. 3 OH^- are added to undercoordinated Ti for charge compensation. The colors of Li, Ti, P, O, and H are green, blue, purple, red, and white, respectively. (b) Formation energy of different surface defects at pH 12 on (012) and (0-14) surfaces. The concentration of Li^+ in solution is set to 0.5 mol L^{-1}, while the concentrations of all other ionic species are set to 10^{-6} mol L^{-1}.

Previous DFT calculations show that the lowest energy surface of LTP and LATP is (012), followed by (0-14),[36,37] which is also verified by our own calculations (Figure S8, Supporting Information). Therefore, we select (012) and (0-14) surfaces as the surfaces on which to study defects. The surface defects considered are: PO_4^{3-} vacancy, Li^+ vacancy, M^{4+} vacancy (M = Ti^{4+} or Ge^{4+}), and Li^+ adsorbate. Li^+ adsorbate defects are only considered on the (012) surface, as half of possible Li sites on the pristine (012) surface are unoccupied to maintain the bulk stoichiometry. In order to simulate the surface degradation in an aqueous solution, the energy of removed or added cations and anions are referenced to the most stable aqueous ionic species as predicted by the ab-initio Pourbaix formalism.[31]

As an example, the formation of a PO_4^{3-} vacancy on the LTP (012) surface is shown in **Figure 5a**, in which a PO_4^{3-} polyanion group is removed from the pristine surface and 3 hydroxyl groups (OH^-) are added to the undercoordinated Ti atoms on the defect surface for charge compensation. Charge compensation by adding OH^- (for PO_4^{3-} vacancy and Li^+ adsorbate) or H^+ (for Li^+, Ti^{4+}, and Ge^{4+} vacancies) to the defect surfaces results in lower defect formation energies than those without (Figure S13, Supporting Information). Hereafter, the superscript for the defect charge is omitted to indicate that all the surface defects are charge compensated.

Figure 5b shows the DFT results for the defect energies on both LTP and LGP surfaces. For both LTP and LGP, the formation of a PO_4 vacancy has the largest driving force, regardless of surface orientation. On the other hand, as shown in Figure 5b, by substituting Ge with Ti, the driving force of PO_4 dissolution is significantly reduced. The PO_4 vacancy formation energy on LTP surfaces is −1.09 and −1.53 eV on (012) and (0–14) surfaces, respectively, which are considerably less negative than the −2.12 and −2.40 eV for LGP surfaces. Such a large difference in the driving force of PO_4 dissolution agrees with our experimental observation that LGP dissolves readily in a high pH solution and forms more Li_3PO_4 precipitates while incorporating Ti can reduce the amount of Li_3PO_4 formed on the surface. Figure 5b highlights another difference between LTP and LGP. While the negative defect formation energies on both (012) and (0–14) surfaces indicate that Ge has a tendency to dissolve, Ti dissolution is thermodynamically unfavorable represented by the positive defect formation energies. This is consistent with the experimental results that Ge dissolves readily, but Ti dissolution cannot be detected. Finally, our calculation also indicates that Li dissolution is not thermodynamically favorable for both LTP or LGP surfaces. In fact, there is a larger tendency to adsorb Li, rather than dissolve Li, from the (012) surface. Therefore, the dissolution of LTP and LGP does not appear to be driven by Li dissolution. In summary, the surface defect calculations indicate that the degradation of LTGP samples in high pH solution is most likely driven by PO_4 dissolution, and further promoted by Ge dissolution in Ge-containing compositions. Substituting Ti for Ge not only reduces the driving force of PO_4 dissolution but also allows Ti to remain on the surface without dissolving.

3. Discussion

In all NASICON samples tested for stability at high pH, large amounts of Li_3PO_4 were precipitated as seen from the decrease in Li^+ and PO_4^{3-} ions in solution observed by ICP-OES (Figure 3c,d)

and the increased Li_3PO_4 phase fraction in XRD (Figure 2b). We found that as more Ti is substituted into the NASICON framework, less Li_3PO_4 is precipitated. This experimental observation agrees with the Pourbaix diagram prediction shown in Figure 1 where Li_3PO_4 is predicted to be a common decomposition product of both LTP and LGP, but LGP has a larger driving force to decompose.

However, despite forming a thick surface layer, the role of Li_3PO_4 in passivation is likely not substantial. Critically, all samples precipitate Li_3PO_4, but only Ti-containing samples exhibit passivation behavior. Therefore, Li_3PO_4 formation does not appear to be a sufficient condition for material passivation. Furthermore, the final amount of Li_3PO_4 formed and a fraction of Ge dissolved is found to decrease with increased Ti content, indicating that Ti-doping is critical to constrain the dissolution of ions.

We rationalize the effect of Ti-substitution in 2 ways. First, changing the metal species at the octahedral site can significantly alter the defect formation energy as shown by our DFT calculations in Figure 5b. The PO_4 vacancy formation in LTP is only half as favorable as in LGP. It is therefore expected that as we substitute more Ge for Ti, the driving force for dissolution will be gradually diminished.

Second, the presence of Ti as an insoluble element enables the formation of Ti-rich solid compounds on the surface which constrain the continued dissolution. In all compositions, no Ti is observed to leach into the solution, despite a large amount of other ions dissolving. This indicates that a Ti-enriched solid phase, possibly TiO_2, must form on the surface. The low Ti concentration in the solution also indicates that the Ti-rich solid phase likely does not form by dissolution-precipitation and instead is formed locally by Ti which is left behind when other ions dissolve. The latter mechanism is also supported by the DFT calculations, which show Ti dissolution is thermodynamically unfavorable. SEM/EDS maps furthermore reveal a diminished Ti signal in the product layer when the Li_3PO_4 layer grows, illustrating that the formation of this Ti-rich solid phase is atop the bulk material but beneath the Li_3PO_4 precipitates. In low Ti-content compositions, each PO_4^{3-} group that dissolves enriches the surface with less Ti than for high Ti compositions, therefore requiring more PO_4^{3-} dissolution to passivate the material with a Ti-rich solid. This larger amount of PO_4^{3-} eventually precipitates as Li_3PO_4, explaining the relationship between higher Li_3PO_4 precipitation and lower Ti content.

In contrast to the insoluble Ti, both ab-initio Pourbaix diagram and experimental ICP measurements indicate that Ge can readily dissolve in the alkaline solution. The formation of solid GeO_2 is even observed for the LGP pellet, which is most likely due to the Ge-ion concentration exceeding its solubility limit.[38]

Interestingly, among all solid decomposition products observed in our experiments (Li_3PO_4, GeO_2, and Ti-rich solid), only the Ti-rich solid effectively passivates the underlying bulk materials. The passivation behavior of the surface Ti-rich solid layer supports the conclusion from previous work[33] —- the formation of solid products on the surface can passivate and stabilize the bulk material, even if the bulk material itself is metastable in the given liquid environment. However, our study also demonstrates that not all solid products are effective in passivation. Specifically, the solid products formed by dissolution-precipitation mechanisms (GeO_2 and Li_3PO_4) do not show a passivating effect in our experiments. One possible explanation is that both GeO_2 and Li_3PO_4 may precipitate at surface locations different from where the dissolution initially occurred, and thus the degraded surface is not effectively protected.

The above observations imply that Li-NASICON materials in an alkaline solution are stabilized via a dissolution-induced passivation mechanism — the phosphate groups and other soluble metals are selectively dissolved, while the insoluble metals remain on the surface and form the passivation layer. The effectiveness of such a passivation mechanism depends on the extent of dissolution required to accumulate enough insoluble elements on the surface. Using the refined Li_3PO_4 weight fractions from XRD and the P-ion concentrations from ICP-OES, we can estimate that 94.0, 36.5, and 28.6 mol% of the PO_4 dissolved after 170 h in LGP, LTGP50, and LTP powder samples, respectively. Evidently, even for LTP, large fractions of the bulk material still dissolve before the material is able to passivate.

Such a passivation mechanism induced by selective dissolution of constituent elements is not unique to the Li-NASICON system. It has been well-studied that the self-passivation of stainless steel relies on the preferential dissolution of Fe, especially in an acidic environment, which results in the enrichment of Cr in the surface oxide layer.[39,40] While the sacrificial dissolution of metals does not cause problems in protecting stainless steel from further corrosion, dissolution is undesirable in a Li-air battery.

In recent work, Kim et al. and Ma et al. observed degraded cell performance when cycling in humidified O_2.[16,41] Both studies observed an increase in porosity of the LATP plate in SEM after a number of cycles. Ma et al. observed a crack formed in the interface between the LATP separator and MEIC cathode, which was identified as the cause for the sudden death of the cell. Decomposition products were also observed clogging the pores of the cathode.

Our fundamental study with LTGP effectively rationalizes these failures. Dissolution of the separator material driven by the PO_4 instability can lead to increased porosity, potentially decreasing both conductivity and mechanical strength, or even resulting in cell failure. Furthermore, the precipitation of Li_3PO_4 is also detrimental in a battery because Li_3PO_4 precipitation may occur on any nearby surface, potentially clogging the porous cathode. These failure modes are schematically drawn in **Figure 6**. By understanding the fundamental mechanisms causing failures in humid cycling conditions, our study highlights the importance of designing Li-air separator materials with strong alkaline stability.

4. Conclusion

In this work, we used XRD, ICP-OES, and SEM/EDS combined with DFT calculations to characterize the morphology and phase of $LiTi_xGe_{2-x}(PO_4)_3$ ($0 \leq x \leq 2$) decomposition products in high alkalinity and demonstrate the degradation mechanism. We found that alkaline instability is driven by the dissolution of the phosphate group which then may reprecipitate as Li_3PO_4. The observed passivation mechanism for compositions that contain Ti appears to be driven by this dissolution which leaves Ti-ions on the surface to create a Ti-rich solid (possibly the TiO_2 (B) phase) passivation layer. When the main metal of the Li-NASICON also dissolves (e.g., Ge), the precipitation of Li_3PO_4 alone does not provide enough protection against continuous dissolution.

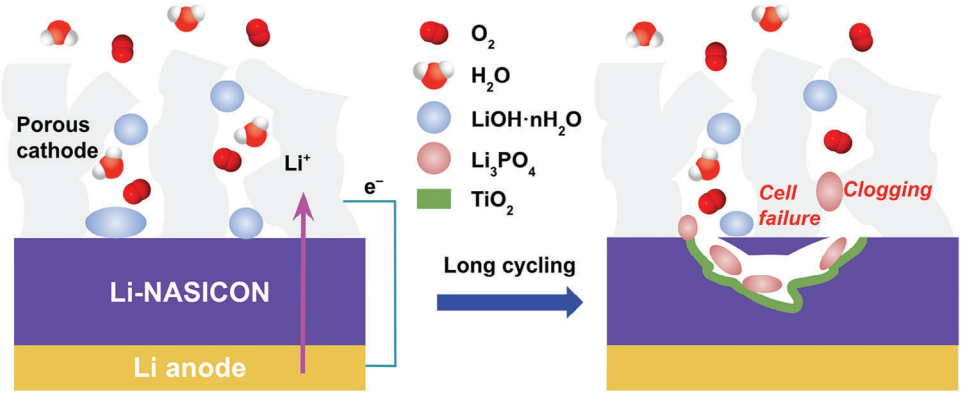

Figure 6. Schematic diagram of (left) a pristine Li-air battery and (right) the failure modes of Li-air batteries operated in humid environments.

Although metal ion substitution toward Ti is shown to reduce the driving force for phosphate dissolution, this effect is insufficient to fully stabilize the material. The bulk Li-NASICON can be stabilized only after a sufficient amount of phosphate groups have dissolved, allowing the Ti-rich solid to passivate the surface. Such a dissolution-induced passivation mechanism is likely to cause adverse effects on the Li-air battery performance in humid air, such as reduced conductivity and cell failure. Further, we speculate that because the PO_4^{3-} dissolution driving force is so strong and is not effectively stopped by metal-ion doping, this alkaline instability may be a general issue for all phosphate-based Li-NASICONs.

5. Experimental Section

Synthesis of Li-NASICON: Five compositions of $LiTi_xGe_{2-x}(PO_4)_3$ (LTGP, x = 0, 0.5, 1.0, 1.5, 2.0) were synthesized with varying amounts of Ti substitution ranging from 0% Ti-substitution to 100% substitution in 25% increments. Samples were made with the solid-state synthesis method previously reported in the literature.[43,44] Li_3CO_3, GeO_2, TiO_2, and $NH_4H_2PO_4$ were mixed in desired stoichiometric ratios. 10% extra Li was added to compensate for Li loss. The precursors were ball-milled in ethanol for 12 h, dried overnight, then calcined at 900 °C for 12 h. Pellets with a diameter of 6 mm were made from this powder and sintered at 1080 °C for 15 h.

Pellet Characterization: Pellet samples were immersed in an alkaline 0.5 mol L^{-1} LiOH solution buffered with 0.25 mol L^{-1} H_3BO_3 (pH 12.3, VWR International) at 70 °C. From preliminary experiments and literature reports, Li-NASICON materials act as acids in solutions to reduce the pH,[45] necessitating a boric acid buffer to control the pH. The pH of 12.3 was chosen because it was within the region of interest on the Pourbaix diagram and maintained a good buffering capacity. The pellets were immersed in the alkaline solution for a cumulative time of 14.5, 32, 48, 70, and 116 h. After each immersion interval, pellets were removed, rinsed with water, and dried in a 70 °C vacuum oven. The rinsing was done to prevent dried LiOH or borates from obscuring the surface.

Scanning electron microscopy paired with energy-dispersive spectroscopy (SEM/EDS, ThermoFisher Phenom XL G2) was used to characterize the surface of each pellet, then the pellet was re-immersed in a fresh alkaline buffer solution for the next immersion interval. Inductively coupled plasma optical emission spectroscopy (ICP-OES, Perkin Elmer 5300 DV) was used to quantify the dissolved ions in the solution. One set of pellets was ground down after 70 h of cumulative immersion and the powder was characterized by X-ray diffraction (XRD). All XRD spectra were collected on a Rigaku MiniFlex 600 diffractometer with Cu-Kα radiation (λ = 1.5406 Å) in the 2θ range 10–70° at a scan rate of 1.5 min.

Powder Characterization: Powder samples of LTGP were also immersed in alkaline solution for 5.4, 9.7, 31, 100, and 172 h. The increased surface area of powders allows for a higher fraction of the material to react and provides a better signal to identify decomposition phases in XRD and resolve ion concentration changes with ICP-OES. The resultant solution was collected for ICP-OES analysis and the solid powder was washed thrice in water, dried in a 70 °C vacuum furnace, then characterized with XRD. In contrast with the pellet samples, each time step is a different sample. Rietveld refinements were performed on the collected powder samples using Profex.[46] LGP and LTGP25 structures were refined to the $LiGe_2(PO_4)_3$ (ICSD coll. code 69 763) structure while LTGP50, LTGP75, and LTP samples were refined to $LiTi_2(PO_4)_3$ (ICSD coll. code 7930). In both cases, the Ti/Ge site occupancy and lattice parameters were allowed to be refined to account for the changes in composition.

Computational Methods: All DFT calculations were performed using the Vienna Ab-Initio Software Package (VASP)[47] within the projector augmented wave (PAW) formalism.[48] Pourbaix diagrams were constructed from ab-initio energies obtained with the r^{2}SCAN functional[49] using the formalism developed by Persson et al.[31] In this approach, the 0K r^{2}SCAN solid phase formation enthalpy is combined with the experimental Gibbs free formation energy of aqueous ions at room temperature. The ionic relaxations were performed with INCAR parameters generated by MPScanRelaxSet implemented in pymatgen.[50] Some solid phases were already optimized with the r^{2}SCAN functional in the Materials Project,[51] and those entries were used without further optimization.

For surface energy calculations, we used the Perdew–Burke–Ernzerhof (PBE) generalized gradient approximation (GGA) functional[52] for higher computational efficiency. Plane-wave basis cutoff energies were set at 520 eV with a Gaussian smearing of 0.05 eV for all calculations. Electronic and ionic optimization convergence criteria are 10^{-5} eV and 0.02 eV Å^{-1}, respectively. Other INCAR parameters and k-point grid were generated by MPRelaxSet implemented in pymatgen. The formation energies of oxides were corrected with the anion correction scheme implemented in pymatgen[53] to account for the GGA error that overbinds the O_2 molecule.

The lattice constants of slabs were first determined by fully relaxing the bulk structures. The unit cell shape of LTP and LGP bulk structures was transformed from the conventional hexagonal cell with R-3c symmetry to the orthorhombic cell, where the planes normal to the a, b, and c axes of the orthorhombic cell are the (0–14), (2-10), and (012) planes of the hexagonal cell, respectively. The optimized lattice constants of the bulk unit cell for LTP and LGP were 8.61 × 8.62 × 12.19 Å and 8.44 × 8.39 × 11.90 Å, respectively. Stoichiometric and symmetric surface slabs were then created with a 15 Å vacuum layer. One of the bulk unit cell axes is set as the surface plane normal and the remaining 2 axes are the in-plane axes. The slab thickness of (012) and (0–14) surfaces for both LTP and LGP slabs are at least 17 Å. The surface energies of pristine surfaces without any surface defects were obtained by fully relaxing atomic positions while fixing the in-plane lattice constants. Defected surfaces were created by removing

or adding atoms symmetrically from both the top and bottom surfaces of the pristine slabs. The atomic positions of outer layers (5–6 Å thick layer on each side of a slab) were fully relaxed for defective surface slabs while keeping the rest of the inner-layer atoms fixed at the same positions as in the pristine surfaces.

Surface defect formation energies were calculated as follows:

$$\Delta E_{defect} = (E_{d-surface} - \Delta N_H \times E_H - \Delta N_O \times E_O - \Delta N_{ion} \times E_{ion} - E_{p-surface})/2 \quad (1)$$

where ΔE_{defect} is surface defect formation energy, $E_{p\text{-}surface}$ is the DFT energy of a pristine surface, and $E_{d\text{-}surface}$ is DFT energy of a defected surface. ΔN_H, ΔN_O, and ΔN_{ion}, are the number of hydrogen, oxygen, and aqueous ions, respectively, added or removed on both sides of the slab to form the surface defects. A positive value indicates the addition of extra atoms, while a negative value indicates removal. E_H, E_O, and E_{ion} are energies of hydrogen, oxygen, and aqueous ions, respectively, which are obtained by applying the same correction scheme as used for constructing the ab-initio Pourbaix diagram.[31] Therefore, the values of E_H, E_O, and E_{ion} are pH, voltage, and ion concentration dependent. All the reference energies for hydrogen, oxygen, and aqueous ions were computed with the PBE functional to be consistent with the slab energies. The factor of 1/2 is due to the symmetrically formed defects on both sides of the slab.

Charge compensation of defect surfaces was achieved by adding OH^- terminations to the defect surface with PO_4^{3-} vacancies or Li^+ adsorbates, and H^+ terminations for all other cation (Li^+, Ti^{4+}, or Ge^{4+}) vacancies. In the case of OH^- terminations, the hydroxyl groups were added to the undercoordinated cations (Li^+, Ti^{4+}, or Ge^{4+}) on the surface. In the case of H^+ terminations, H atoms were added to the dangling O atoms that were originally bonded to the removed cation (Li^+, Ti^{4+}, or Ge^{4+}). We enumerated all possible OH^-/H^+ terminations for each type of defect based on the above rules, and the lowest energy is chosen for the defect formation energy of its kind. The lowest energy surface configurations for each type of surface defect on LTP and LGP surfaces are shown in Supporting Information Figures S9–S12 (Supporting Information). All structures were visualized using VESTA.[54]

Supporting Information

Supporting Information is available from the Wiley Online Library or from the author.

Acknowledgements

This work was supported by the Samsung Advanced Institute of Technology (SAIT). The computational analysis was performed using computational resources sponsored by the Department of Energy's Office of Energy Efficiency and Renewable Energy located at the National Renewable Energy Laboratory (NREL). Computational resources were also provided by the Advanced Cyberinfrastructure Coordination Ecosystem: Services & Support (ACCESS) program, which is supported by National Science Foundation grants #2138259, #2138286, #2138307, #2137603, and #2138296.

Conflict of Interest

The authors declare no conflict of interest.

Author Contributions

B.X.L. and Z.L. contributed equally to this work. B.X.L. conducted all experimental works. Z.L. performed DFT calculations. T.P.M. participated in the discussion of this work. The manuscript was written by B.X.L. and Z.L., and revised by G.C. The work was supervised by G.C.

Data Availability Statement

The data that support the findings of this study are available from the corresponding author upon reasonable request.

Keywords

alkaline stability, DFT simulations, Li-air Battery, Li-NASICON, solid state conductors

Received: August 12, 2024
Revised: October 17, 2024
Published online:

[1] H. Au, M. Crespo-Ribadeneyra, M.-M. Titirici, *One Earth* **2022**, *5*, 207.
[2] T. Liu, J. P. Vivek, E. W. Zhao, J. Lei, N. Garcia-Araez, C. P. Grey, *Chem. Rev.* **2020**, *120*, 6558.
[3] G. Girishkumar, B. McCloskey, A. C. Luntz, S. Swanson, W. Wilcke, *J. Phys. Chem. Lett.* **2010**, *1*, 2193.
[4] L. Liu, H. Guo, L. Fu, S. Chou, S. Thiele, Y. Wu, J. Wang, *Small* **2021**, *17*, 1903854.
[5] A. C. Luntz, B. D. McCloskey, *Chem. Rev.* **2014**, *114*, 11721.
[6] S. Meini, M. Piana, N. Tsiouvaras, A. Garsuch, H. A. Gasteiger, *Electrochem. Solid-State Lett.* **2012**, *15*, A45.
[7] T. Liu, M. Leskes, W. Yu, A. J. Moore, L. Zhou, P. M. Bayley, G. Kim, C. P. Grey, *Science* **2015**, *350*, 530.
[8] Z. Guo, X. Dong, S. Yuan, Y. Wang, Y. Xia, *J. Power Sources* **2014**, *264*, 1.
[9] K. U. Schwenke, M. Metzger, T. Restle, M. Piana, H. A. Gasteiger, *J. Electrochem. Soc.* **2015**, *162*, A573.
[10] D. G. Kwabi, T. P. Batcho, S. Feng, L. Giordano, C. V. Thompson, Y. Shao-Horn, *Phys. Chem. Chem. Phys.* **2016**, *18*, 24944.
[11] N. B. Aetukuri, B. D. McCloskey, J. M. García, L. E. Krupp, V. Viswanathan, A. C. Luntz, *Nat. Chem.* **2015**, *7*, 50.
[12] Y. G. Zhu, Q. Liu, Y. Rong, H. Chen, J. Yang, C. Jia, L.-J. Yu, A. Karton, Y. Ren, X. Xu, S. Adams, Q. Wang, *Nat. Commun.* **2017**, *8*, 14308.
[13] P. Tan, W. Shyy, T. S. Zhao, R. H. Zhang, X. B. Zhu, *Appl. Energy* **2016**, *182*, 569.
[14] F. Li, S. Wu, D. Li, T. Zhang, P. He, A. Yamada, H. Zhou, *Nat. Commun.* **2015**, *6*, 7843.
[15] S. Ma, J. Wang, J. Huang, Z. Zhou, Z. Peng, *J. Phys. Chem. Lett.* **2018**, *9*, 3333.
[16] M. Kim, H. Lee, H. J. Kwon, S.-M. Bak, C. Jaye, D. A. Fischer, G. Yoon, J. O. Park, D.-H. Seo, S. B. Ma, D. Im, *Sci. Adv.* **2022**, *8*, eabm8584.
[17] M. Takeuchi, R. Kurosawa, J. Ryu, M. Matsuoka, *ACS Omega* **2021**, *6*, 33075.
[18] D. D. Williams, R. R. Miller, *Ind. Eng. Chem. Fund.* **1970**, *9*, 454.
[19] H. Kim, H. Lee, W. Choi, G. Yoon, C. Jung, M. Kim, T. Kim, J. Park, D. Im, *ACS Appl. Mater. Interfaces* **2023**, *15*, 29120.
[20] C. Monnin, M. Dubois, *J. Chem. Eng. Data* **2005**, *50*, 1109.
[21] N. Imanishi, S. Hasegawa, T. Zhang, A. Hirano, Y. Takeda, O. Yamamoto, *J. Power Sources* **2008**, *185*, 1392.
[22] S. Hasegawa, N. Imanishi, T. Zhang, J. Xie, A. Hirano, Y. Takeda, O. Yamamoto, *J. Power Sources* **2009**, *189*, 371.
[23] H. Al-Salih, M. S. E. Houache, E. A. Baranova, Y. Abu-Lebdeh, *Adv. Energy Sustain. Res.* **2022**, *3*, 2200032.
[24] T. Zhang, H. Zhou, *Nat. Commun.* **2013**, *4*, 1817.
[25] R. Chen, Q. Li, X. Yu, L. Chen, H. Li, *Chem. Rev.* **2020**, *120*, 6820.
[26] Y. Shimonishi, T. Zhang, N. Imanishi, D. Im, D. J. Lee, A. Hirano, Y. Takeda, O. Yamamoto, N. Sammes, *J. Power Sources* **2011**, *196*, 5128.
[27] K. He, C. Zu, Y. Wang, B. Han, X. Yin, H. Zhao, Y. Liu, J. Chen, *Solid State Ionics* **2014**, *254*, 78.

[28] K. B. Dermenci˙, *Int. J. Autom. Sci. Technol.* **2020**, *4*, 295.
[29] A. Rossbach, F. Tietz, S. Grieshammer, *J. Power Sources* **2018**, *391*, 1.
[30] V. Diez-Gómez, K. Arbi, J. Sanz, *J. Am. Chem. Soc.* **2016**, *138*, 9479.
[31] K. A. Persson, B. Waldwick, P. Lazic, G. Ceder, *Phys. Rev. B* **2012**, *85*, 235438.
[32] C. Xiao, L. Zeng, *Hydrometallurgy* **2018**, *178*, 283.
[33] A. K. Singh, L. Zhou, A. Shinde, S. K. Suram, J. H. Montoya, D. Winston, J. M. Gregoire, K. A. Persson, *Chem. Mater.* **2017**, *29*, 10159.
[34] W. Sun, D. A. Kitchaev, D. Kramer, G. Ceder, *Nat. Commun.* **2019**, *10*, 573.
[35] T. P. Feist, P. K. Davies, *J. Solid State Chem.* **1992**, *101*, 275.
[36] M. A. Pogosova, I. V. Krasnikova, A. O. Sanin, S. A. Lipovskikh, A. A. Eliseev, A. V. Sergeev, K. J. Stevenson, *Chem. Mater.* **2020**, *32*, 3723.
[37] H.-K. Tian, Z. Liu, Y. Ji, L.-Q. Chen, Y. Qi, *Chem. Mater.* **2019**, *31*, 7351.
[38] P. A. Nikolaychuk, *Phosphorus, Sulfur, Silicon Related Elem.* **2023**, *198*, 705.
[39] X. Wang, D. Mercier, S. Zanna, A. Seyeux, L. Perriere, M. Laurent-Brocq, I. Guillot, V. Maurice, P. Marcus, *Npj Mater. Degrad.* **2023**, *7*, 1.
[40] V. Maurice, P. Marcus, *Curr. Opinion Solid State Mater. Sci.* **2018**, *22*, 156.
[41] S. B. Ma, H. J. Kwon, M. Kim, S. Bak, H. Lee, S. N. Ehrlich, J. Cho, D. Im, D. Seo, *Adv. Energy Mater.* **2020**, *10*, 2001767.
[42] S. D. Jackman, R. A. Cutler, *J. Power Sources* **2013**, *230*, 251.
[43] K. Arbi, S. Mandal, J. M. Rojo, J. Sanz, *Chem. Mater.* **2002**, *14*, 1091.
[44] H. Aono, E. Sugimoto, Y. Sadaoka, N. Imanaka, G. Adachi, *J. Electrochem. Soc.* **1990**, *137*, 1023.
[45] D. Safanama, S. Adams, *J. Power Sources* **2017**, *340*, 294.
[46] N. Doebelin, R. Kleeberg, *J. Appl. Cryst.* **2015**, *48*, 1573.
[47] G. Kresse, J. Furthmüller, *Phys. Rev. B* **1996**, *54*, 11169.
[48] G. Kresse, D. Joubert, *Phys. Rev. B* **1999**, *59*, 1758.
[49] J. W. Furness, A. D. Kaplan, J. Ning, J. P. Perdew, J. Sun, *J. Phys. Chem. Lett.* **2020**, *11*, 8208.
[50] S. P. Ong, W. D. Richards, A. Jain, G. Hautier, M. Kocher, S. Cholia, D. Gunter, V. L. Chevrier, K. A. Persson, G. Ceder, *Comput. Mater. Sci.* **2013**, *68*, 314.
[51] R. S. Kingsbury, A. S. Rosen, A. S. Gupta, J. M. Munro, S. P. Ong, A. Jain, S. Dwaraknath, M. K. Horton, K. A. Persson, *npj Comput. Mater.* **2022**, *8*, 195.
[52] J. P. Perdew, K. Burke, M. Ernzerhof, *Phys. Rev. Lett.* **1996**, *77*, 3865.
[53] A. Wang, R. Kingsbury, M. McDermott, M. Horton, A. Jain, S. P. Ong, S. Dwaraknath, K. A. Persson, *Sci. Rep.* **2021**, *11*, 15496.
[54] F. Izumi, K. Momma, *J Appl Cryst* **2011**, *44*, 1272.